



A thermodynamic and crystal structure study of thermally aged lithium ion cells



Kenza Maher^{a,b,*}, Rachid Yazami^{a,b,*}

^aNanyang Technological University, School of Materials Science and Engineering and Energy, Research Institute at NTU (ERIAN), 1 CleanTech Loop, #06-04, CleanTech One, Singapore 637141, Singapore

^bTUM CREATE, 1 Create Way, #10-02 Create Tower, Singapore 138602, Singapore

HIGHLIGHTS

- Effect of thermal ageing on cells' thermodynamic and kinetic properties.
- Degradation of electrochemical performance with the ageing temperature and time.
- Strong correlation between cells thermodynamic changes and electrodes degradation.
- Thermodynamics method allows a distinction between different ageing modes.

ARTICLE INFO

Article history:

Received 13 November 2013

Received in revised form

18 December 2013

Accepted 19 December 2013

Available online 18 January 2014

Keywords:

Lithium ion batteries

Electrode materials degradation

Thermal ageing

Thermodynamics

Entropy

Enthalpy

ABSTRACT

Lithium ion batteries in the coin-cell form factor (2032) initially charged to 4.2 V at ambient temperature are stored at 60 °C and 70 °C for up to 8 weeks. The cells discharge capacity (Q_d) and thermodynamic properties, including open-circuit potential (OCP), entropy (ΔS) and enthalpy (ΔH) are measured after each completed ageing week. Post-mortem analysis of aged anodes and cathodes is investigated by X-ray diffractometry (XRD) and Raman Scattering spectrometry (RS) in an attempt to correlate thermodynamic data to changes in the crystal structure characteristics. It is found that degradation of the electrode materials' crystal structure accounts for most of the observed changes in the cells' thermodynamics with well quantified and distinct contributions from anode and cathode.

© 2014 Elsevier B.V. All rights reserved.

1. Introduction

There are several well established causes of performance degradation of lithium ion batteries (LiB) including long charge/discharge cycling [1–3], thermal ageing [4–13], high rate charge and discharge [14–16], overcharging [17–20] and over discharging [17]. Performance degradation includes decays in discharge capacity, in discharge potential [21–23] and in power output [4,10,21]. Cells performance decays relate to irreversible changes in

the anode, the cathode and the electrolyte physical properties such as crystal structure degradation in anode [24–26] and cathode [26–28] and in the electrode/electrolyte interfacial properties [29–31]. Other processes such as metal dissolution [32–34], electrolyte decomposition [35–39] and electrode mechanical properties degradation due to active materials electrical disconnection from the current collector [40] may also account for battery decaying performances.

In a recent study we investigated the effect of overcharge and long cycling of LiB cells on electrochemical performances and on thermodynamics properties [41,42]. We assigned the cells' performance decay to crystal structure degradation of the cathode and anode materials, which correlate well with changes in the entropy and enthalpy profiles. In this study we investigate the effect of high temperature ageing on the cells' thermodynamic and kinetic

* Corresponding authors. Nanyang Technological University, School of Materials Science and Engineering and Energy, Research Institute at NTU (ERIAN), 1 CleanTech Loop, #06-04, CleanTech One, Singapore 637141, Singapore.

E-mail addresses: kmaher@ntu.edu.sg, kenza.maher@tum-create.edu.sg (K. Maher), rachid@ntu.edu.sg (R. Yazami).

properties. This includes open-circuit potential (OCP), entropy and enthalpy profiles, discharge capacity, average discharge potential and energy output.

A new thermodynamics based approach will be introduced in this paper. It enables a clear distinction between contribution to the cell performance decay arising from anode and cathode [43]. Post-mortem analyses of anode and cathode materials by XRD and RS support the point that crystal structure degradation is the main cause of the changes in the cells' thermodynamic and kinetic properties in thermally aged cells.

2. Experimental

2.1. Storage condition and capacity loss determination

LiB coin cells' (2023) of initial capacity $Q_0 \sim 44$ mAh are used in this study.

The cells were conditioned, aged and tested according to the following steps:

- A charge to 4.2 V under 10 mA constant current ($\sim C/4$ -rate) at ambient temperature using an Arbin Instruments battery cyclizer.
- A thermal storage of charged cells at $60^\circ\text{C} \pm 1^\circ\text{C}$ and $70^\circ\text{C} \pm 1^\circ\text{C}$ for a period up to 8 weeks.
- Four cells were retrieved at completion of each week and naturally cooled to the ambient temperatures.
- The four cells are then charged to 4.2 V and discharged to 2.75 V under ± 10 mA, a step in which the cells' discharge capacity $Q_d(T_s, n)$, capacity loss $(Q_0 - Q_d(T_s, n))/Q_0 \times 100$ (in %), and average discharge potential $\langle e_d(T_s, n) \rangle$ are assessed, where n = number of ageing weeks ($0 \leq n \leq 8$; $n = 0$) corresponds to a fresh cell) and T_s = the storage temperature).

The cells discharge energy ' E ' is then assessed using Eq. (1):

$$E(T_s, n) = Q_d(T_s, n) \times \langle e_d(T_s, n) \rangle \quad (1)$$

2.2. Thermodynamics measurements

The four discharged cells of step iv. are transferred into the Electrochemical Thermodynamics Measurement System (ETMS, BA-2000®, KVI PTE LTD, Singapore) then the following processes are carried out:

- Conditioning cycle: cells are charged to 4.2 V under 9 mA then a constant 4.2 V voltage is applied until the charge current dropped below 0.05 mA. Cells are then discharged to 2.75 V under 9 mA and constant 2.75 V voltage is held until the discharge current dropped below 0.05 mA. In these steps the ETMS assesses the cells' charge and discharge capacity, which is close to $Q_d(T_s, n)$.
- Electrochemical thermodynamics measurements (ETM) test: discharged cells are charged at $C/6$ -rate for 18 min corresponding to 5% increment in state of charge (Σ). Therefore, after the j th charge increment the cells' state of charge Σ_j is given by: $\Sigma_j (\%) = 5j$ ($1 \leq j \leq 20$).
- At Σ_j the cells temperature T is decreased from ambient ($\sim 25^\circ\text{C}$) to 10°C by 5°C steps while keeping the circuit open and monitoring the OCP. Each T is kept constant for 30 min and the cells' OCP ' $E_0(\Sigma_j, T)$ ' is measured. Typically, after 30 min relaxation time $E_0(\Sigma_j, T)$ varies by less than

$40 \mu\text{V min}^{-1}$, which is considered close enough to thermodynamic equilibrium.

From linearity of $E_0(\Sigma_j, T)$ vs. T in step iii., the ETM system automatically determines the entropy $\Delta S(\Sigma_j)$ and the enthalpy $\Delta H(\Sigma_j)$ according to Eqs. (2) and (3), respectively

$$\Delta S(\Sigma_j) = \frac{\partial S(\Sigma_j)}{\partial \Sigma_j} = F \frac{\partial E_0(\Sigma_j, T)}{\partial T} \quad (2)$$

$$\Delta H(\Sigma_j) = \frac{\partial H(\Sigma_j)}{\partial \Sigma_j} = F \left(E_0(\Sigma_j, T) - T \frac{\partial E_0(\Sigma_j, T)}{\partial T} \right), \quad (3)$$

where $\partial S(\Sigma_j)/\partial \Sigma_j$ and $\partial H(\Sigma_j)/\partial \Sigma_j$ are, respectively, the slope of S and H vs. Σ_j at well-defined Σ_j .

By iteration of steps i. to iii., twenty one entropy and enthalpy data points are acquired and plotted vs. Σ_j and vs. OCP.

2.3. Post-mortem crystal structure analyses

At the last charge increment of step iii. ($j = 20$), one or two cell samples are retrieved from the ETMS and discharged to 2.75 V at 10 mA then opened in a glove box filled with argon. The anode and the cathode are separated and washed with DMC of 99% purity used as received, then dried in argon at ambient temperatures and in vacuum at 60°C for about 1 h.

The anode and cathode samples are analysed by XRD (Bruker D8 Advance diffractometer) using CuK_α radiation in the angular range of 15° – 90° (2θ) for cathode and 20° – 90° (2θ) for anode with 0.02° 2θ -steps and by RS (Renishwa inVia Raman microscope) in the backscattering geometry; with the 514 nm radiation by an argon ion laser of 20 mW power.

3. Results and discussion

3.1. Thermodynamics and kinetics data

3.1.1. Initial OCP and discharge data

The cells' OCP measured at ambient temperature immediately after ageing at 60°C and 70°C is plotted versus the ageing time in Fig. 1A, a and b, respectively. The two traces almost lie on the top of each other for the first 5 ageing weeks. Then they split from each other as cells aged at 70°C feature a sharp decrease in OCP compared to those aged at 60°C . The corresponding discharge capacity ($Q_d(T_s, n)$) profiles are plotted in Fig. 1B, a and b, respectively. For the first two weeks the $Q_d(T_s, n)$ traces are quite close to each other. Only after the third week they depart as the capacity of cells aged at 70°C becomes increasingly lower than the ones aged at 60°C .

From an initial discharge capacity of 44 mAh in fresh cells, the discharge capacity dropped to about 37 mAh and 32.5 mAh after 8 ageing weeks at 60°C and 70°C , respectively, corresponding to irreversible capacity losses of 15.9% and 26.1%, respectively. It is generally admitted that above *circa* 20% capacity loss, a LiB is considered no more operational, which is the case of the cells aged at 70°C for 8 weeks.

Fig. 1C, a and b shows the average discharge potential $\langle e_d(T_s, n) \rangle$ profiles of cells aged at 60°C and 70°C , respectively. $\langle e_d(T_s, n) \rangle$ is defined in Eq. (4):

$$\langle e_d(T_s, n) \rangle = \frac{1}{t_d} \int_0^{t_d} e(t) dt, \quad (4)$$

where $e(t)$ = time dependent cell discharge voltage and t_d = total discharge time. Fig. 1D, a and b shows the corresponding energy

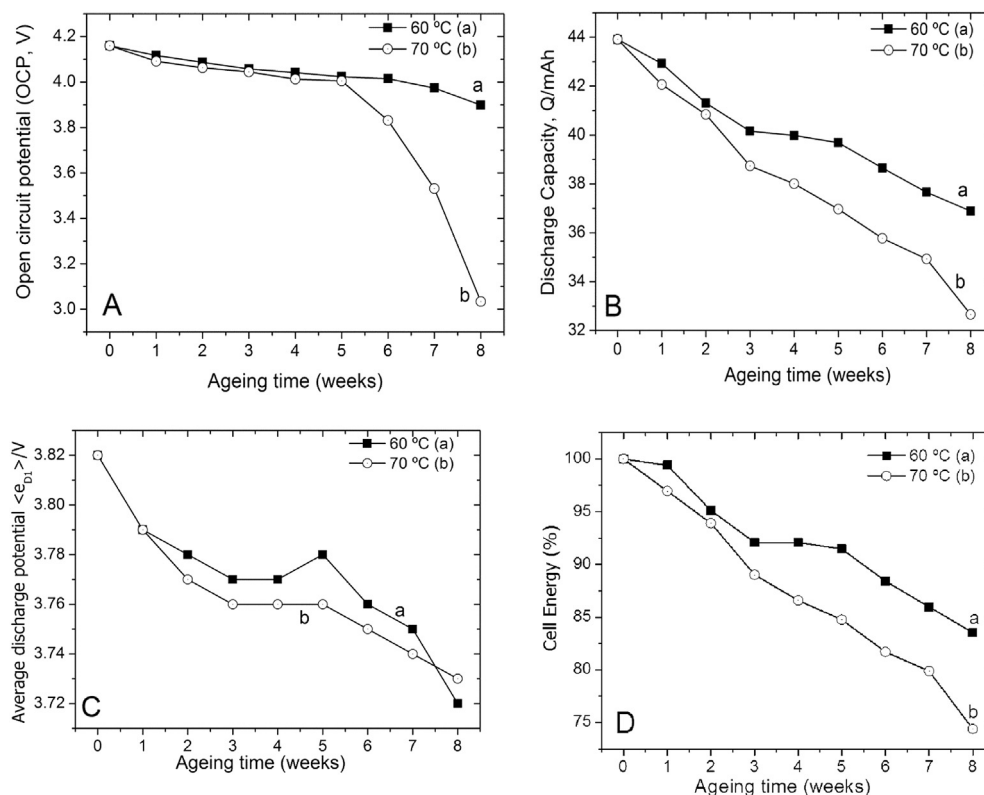


Fig. 1. Ageing time dependence at 60 °C and 70 °C of LiB cells of: (A) Open-circuit potential (OCP), (B) discharge capacity, (C) average discharge potential and, (D) Discharge energy.

profile (as defined in Eq. (1)). As expected, with increasing ageing time, cells aged at 60 °C show higher discharge potential and discharge energy than those aged at 70 °C.

As discussed in the following sections a decay in both discharge capacity and discharge potential relates to degradation of electrode materials and/or electrolyte [11,16,26,39] and to altered electrode/electrolyte interfacial charge transport properties [27,38,39], which leads to increased cells' internal resistance. These changes affect the cells' state of health (SOH), which may be defined in relation with energy loss, shown in Fig. 1D, a and b.

$$\text{SOH} = 100 - \text{Energy Loss} \quad (\%) \quad (5)$$

Fig. 2 shows OCP profiles during charge and discharge of fresh cells vs. Σ . Noteworthy is the quasi absence of any hysteresis between the charge and the discharge traces. This indicates that the ETM operation parameters (charge and discharge current and OCP relaxation time) were chosen within a good range and that the ETM results are highly consistent and reproducible. Therefore, we applied the same ETM protocol for all cells of this study and will show OCP data during charge only.

The OCP traces in Fig. 2 show a steep change in slope at $\Sigma = 5\%$ and lesser changes at around 25% and 45%. There is no noticeable change in slope at other Σ values in particular at 80%, a result in contrast with the entropy and the enthalpy data shown in the next section.

Fig. 3A and B displays the OCP profiles vs. Σ of cells aged at 60 °C and 70 °C for 8 weeks, respectively. OCP curves in Fig. 3A lay on top of each, except at 0% Σ value. OCP data dispersion at $\Sigma = 0\%$ may be due to residual lithium in the graphite anode at the end of discharge, which strongly affects the anode thermodynamic state. In contrast with the data achieved at 60 °C, Fig. 3B shows larger OCP data dispersion with ageing time at 70 °C. This suggests a deeper

cells' degradation has taken place during ageing at 70 °C as compared to 60 °C.

3.1.2. Entropy and enthalpy

3.1.2.1. Results

3.1.2.1.1. Fresh cells. The entropy profiles of fresh cells versus Σ and OCP are plotted in Fig. 4A and B, respectively and the corresponding enthalpy profiles are displayed in Fig. 5A and B, respectively. In Figs. 4A, B and 5A, B particular data points labelled A₁, A₂ and C₁ to C₅, have been found. These particular data points are associated with onsets of phase transitions in the graphite anode (A₁, A₂) and in the LCO cathode (C₁ to C₅) as discussed later.

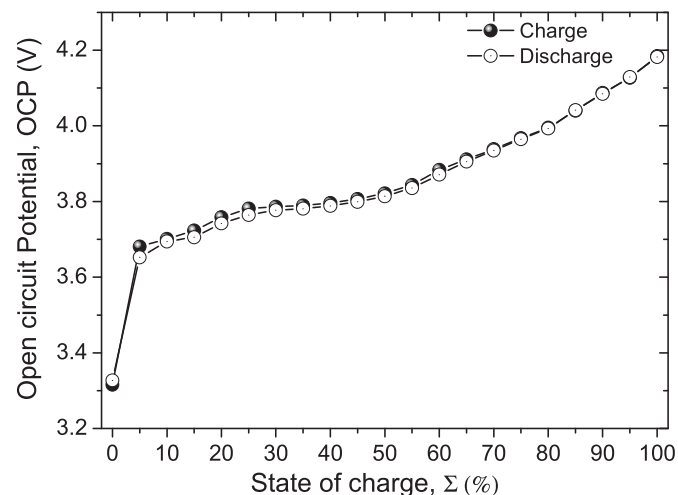


Fig. 2. Open circuit potential profile of fresh (un-aged) LiB cells during charge and discharge vs. state of charge (Σ).

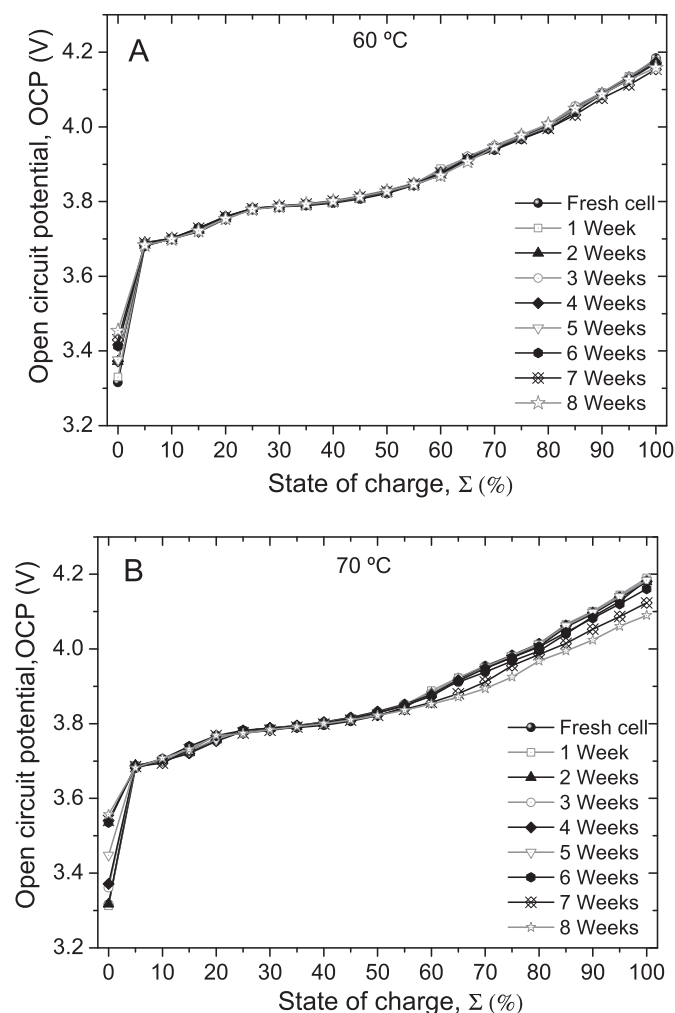


Fig. 3. Open circuit potential profile vs. Σ of LiB cells aged at (A) 60 °C and, (B) 70 °C.

Since similar features are observed in ΔS and ΔH profiles plotted vs. Σ and vs. OCP, only data plotted vs. OCP will be presented in the following sections to avoid redundancy.

3.1.2.1.2. Aged cells. Entropy profiles of cells aged at 60 °C and 70 °C as function of OCP are displayed in Fig. 6A and B, respectively and the corresponding enthalpy profiles are displayed in Fig. 7A and B, respectively. To highlight the ageing time effect on entropy and enthalpy, the profiles of a fresh cell and a cell aged for 8 weeks are shown in the inserts of Figs. 6 and 7 in the OCP range 3.85 V–4.15 V where entropy and enthalpy changes are found to be more significant.

The most noticeable changes in ΔS and ΔH data occur at OCP around 4 V and 3.68 V. These particular OCP values correspond to C_4 and A_1 data points, respectively. The peak at C_4 decreased in intensity, shifted to higher potentials and flattened. In the meantime, the intensity of the peak at A_1 increased.

Because of a higher sensitivity to thermal ageing A_1 and C_4 data points will be used to track the evolution of entropy and enthalpy of anode and cathode, respectively.

Fig. 8A and B shows the ageing time dependence of entropy (a) and enthalpy (b) of cells aged at 60 °C at A_1 and C_4 data points, respectively and Fig. 9A and B show similar data for cells aged at 70 °C. The entropy and enthalpy profiles at A_1 are quite different from those at C_4 for both ageing temperatures. Fig. 8A shows a quasi-linear behaviour of entropy and enthalpy for A_1 at 60 °C. For C_4 , however, entropy keeps almost constant during the first 5

weeks and then it drops dramatically for the last 3 weeks (Fig. 8Ba). Concomitantly, the enthalpy profile drops quasi linearly with ageing time (Fig. 8Bb).

Fig. 9A at 70 °C shows an overall increase of entropy and enthalpy at A_1 except between weeks 2 and 4 where both remained almost constant. For C_4 , however, entropy makes a plateau during the first two weeks and then it drops sharply during the following week and keeps dropping more smoothly for the 5 last weeks (Fig. 9Ba). Enthalpy at C_4 in Fig. 9Bb follows almost the same trends than entropy except it decreases during the first week before making a semi-plateau between weeks 3 and 7 then it drops for the last week.

3.1.2.2. Discussion

3.1.2.2.1. Fresh cells. When comparing Fig. 2 and Figs. 4A and 5A of OCP, entropy and enthalpy profiles vs. Σ of fresh cells, respectively, more features can be found in the entropy and enthalpy profiles as compared to the OCP one. Data points A_1 , A_2 and C_1 to C_5 in Figs. 4 and 5 can be assigned to onsets of phase transitions in the anode (A_i) and cathode (C_i), respectively. In a previous study on Li/graphite and Li/LCO half cells [43], we reported on particular Σ values where entropy profiles shows noticeable changes in slope. In the graphite anode a steep drop and a jump in entropy occur around $\text{Li}_{0.05}\text{C}_6$ and $\text{Li}_{0.5}\text{C}_6$ compositions, respectively. These features are respectively associated to phase transitions from graphite

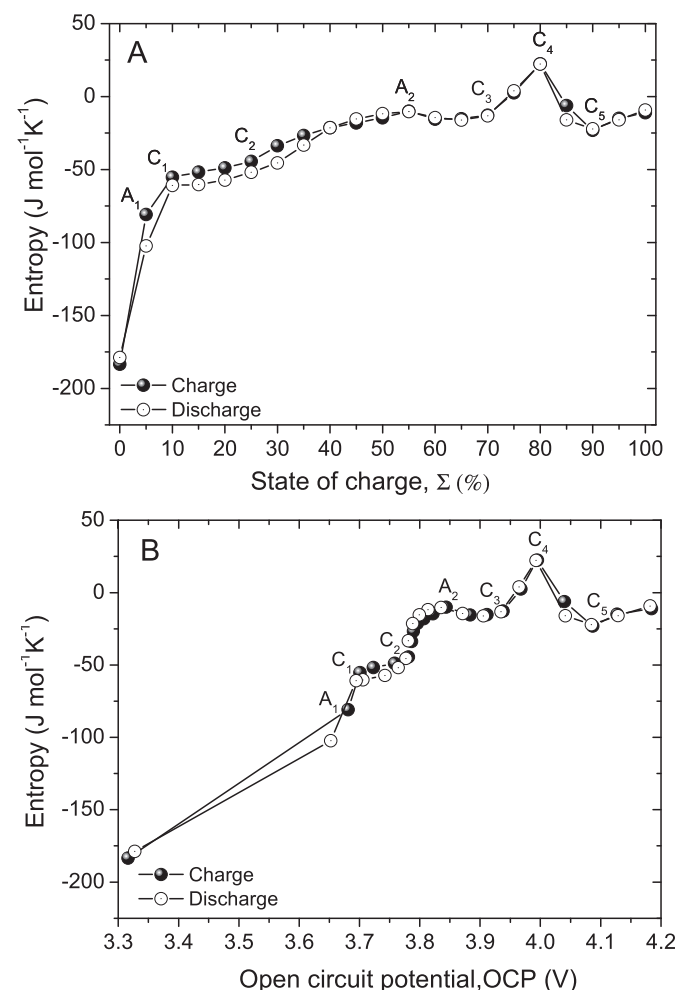


Fig. 4. Entropy profile of LiB fresh cells during charge and discharge (A) vs. Σ and, (B) vs. OCP.

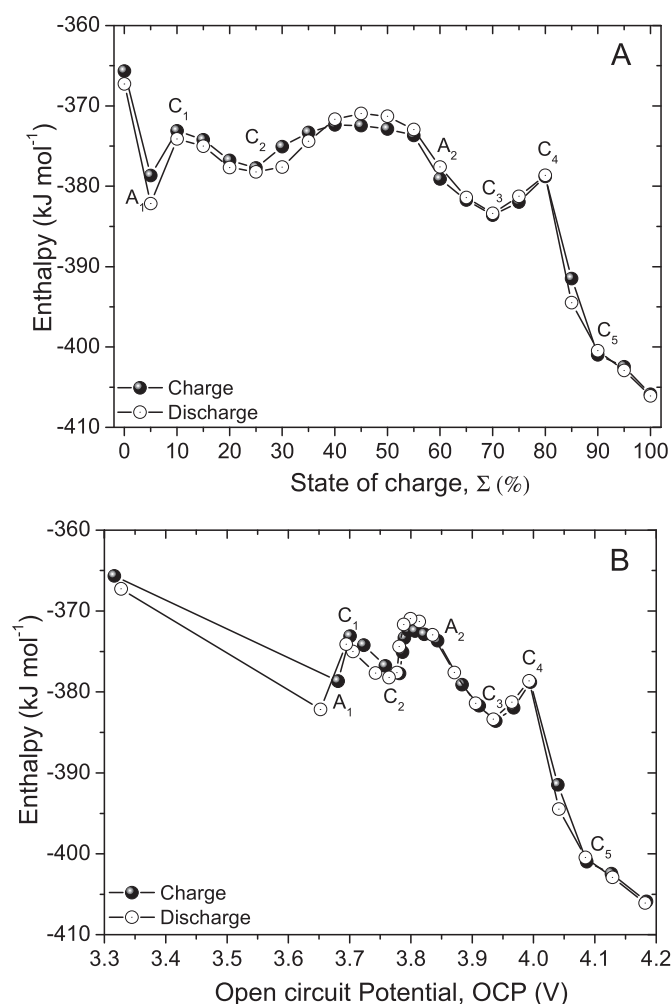


Fig. 5. Enthalpy profile of LiB fresh cells during charge and discharge (A) vs. Σ and, (B) vs. OCP.

to diluted stage 1 and from stage 2 to stage 1 in lithiated graphite [44,45].

In Li/LCO half cells successive phase transitions from initial hexagonal phase (Hex) (O3 of Li₁CoO₂ composition) in the discharged state to monoclinic (Mon) phase in the fully charged state at 4.2 V vs. Li⁺/Li of \sim Li_{0.5}CoO₂ composition [46] take place as follows:

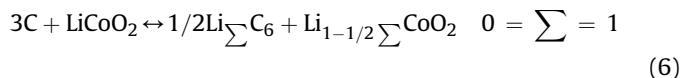
- C₁: Single phase (Hex O3I) \rightarrow Two-phase (O3I + O3II) at \sim Li_{0.95}CoO₂,
- C₂: Two-phase (O3I + O3II) \rightarrow Single phase (O3II) at \sim Li_{0.875}CoO₂,
- C₃: Single phase (O3II) \rightarrow Single monoclinic phase (Mon) at \sim Li_{0.65}CoO₂,
- C₄: Mon \rightarrow Hex (O3II') at \sim Li_{0.6}CoO₂, and
- C₅: Hex (O3II') \rightarrow Hex (O3) at \sim Li_{0.55}CoO₂.

Onsets of phase transitions in anode and cathode are specific to each one of the materials. The occurrence of particular data points A₁ and A₂ and C₁ to C₅ in the entropy and enthalpy profiles is the thermodynamics evidence that the chemistry of LiB used in this study consists of graphite anode and LCO cathode. This statement will be later confirmed by post mortem XRD and RS analyses.

LiB cells are generally anode and cathode balanced by construction to insure no excess anode or cathode is used to optimize

energy density. In an ideally balanced cell, the cells' capacity should be equal to the one of the anode and to the one of the cathode. Accordingly, the full cell state of charge should be equal to the one of the anode and to the one of the cathode.

In a graphite/LCO balanced cell, the cell reaction at each state of charge Σ is ideally schematized by the equation:



Because 1) entropy (and enthalpy) of a full cell is the difference between entropy (and enthalpy) of cathode and anode and, 2) phase transition in anode and cathode take place at well-defined Σ_{anode} and $\Sigma_{cathode}$, respectively, any phase transition in either electrode will have a signature in the entropy and enthalpy profiles of the full cell at that particular cell's Σ value. This statement accounts for the presence of A₁, A₂ and C₁ to C₅ data points in entropy and enthalpy profiles in Figs. 4 and 5. In fact, a detailed analysis of the A₁, A₂ and C₁ to C₅ position should allow one to determine whether the cell is cathode and anode balanced or not. The cathode vs. anode mass balance assessment is beyond the current study and will be presented in a future paper.

3.1.2.2.2. Aged cells. The data in Fig. 6A and B on the one hand and in Fig. 7A and B on the other hand clearly show that entropy and enthalpy profiles are strongly affected by the ageing temperature and time. This is more visible in the OCP area of inserts in Figs. 6 and 7 between 3.85 V and 4.15 V.

Changes in thermodynamic properties with ageing temperature and time displayed in Figs. 6–9 support a model following which electrochemically active electrode materials in anode and cathode gradually convert to less active (or inactive) materials upon ageing. The presence of less active (or inactive) component in anode and cathode should account for irreversible capacity losses in the electrode and, therefore, in the full cell. Moreover, only lithium stoichiometry in the active component of anode and cathode controls its potential and capacity. Accordingly, the thermodynamic behaviour of the full cell relates to the active component of each one of the electrodes. Since onsets of phase transitions will take place at well-defined lithium compositions (and potentials) in the active component of the electrodes only, changes in entropy and enthalpy profiles during thermal ageing in particular at A₁ and C₄ should be associated with changes in the thermodynamic properties of graphite anode and the LCO cathode, respectively.

The quasi-linear increase in entropy and enthalpy of anode shown in Figs. 8A and 9A at 60 °C and 70 °C, respectively suggests the anode degrades starting from the beginning of ageing and changes in entropy and enthalpy in anode are somehow correlated. This feature contrasts with the one of the LCO cathode. In fact, as shown in Figs. 8B and 9B LCO degradation takes place stepwise, suggesting some level of resilience and/or higher activation energy for irreversible decomposition reactions. Moreover changes in entropy and enthalpy are less correlated in LCO than in the graphite anode. A less correlated entropy and enthalpy in LCO suggests differences in the mechanism of the cathode degradation as sensed by entropy and enthalpy state functions. Configurational (mixing) entropy, which is the major component of entropy in chemical systems (as compared to vibrational, electronic and nuclear entropy) [47], is highly sensitive to crystal structure and electronic structure disorder in the LCO material. Enthalpy, however, should be associated with changes in inter-atomic bonds such as Li–O and Co–O bonds following reversible (Li⁺ intercalation/de-intercalation) and irreversible (bonds breaking and re-formation) processes, which account for the major part of the total free

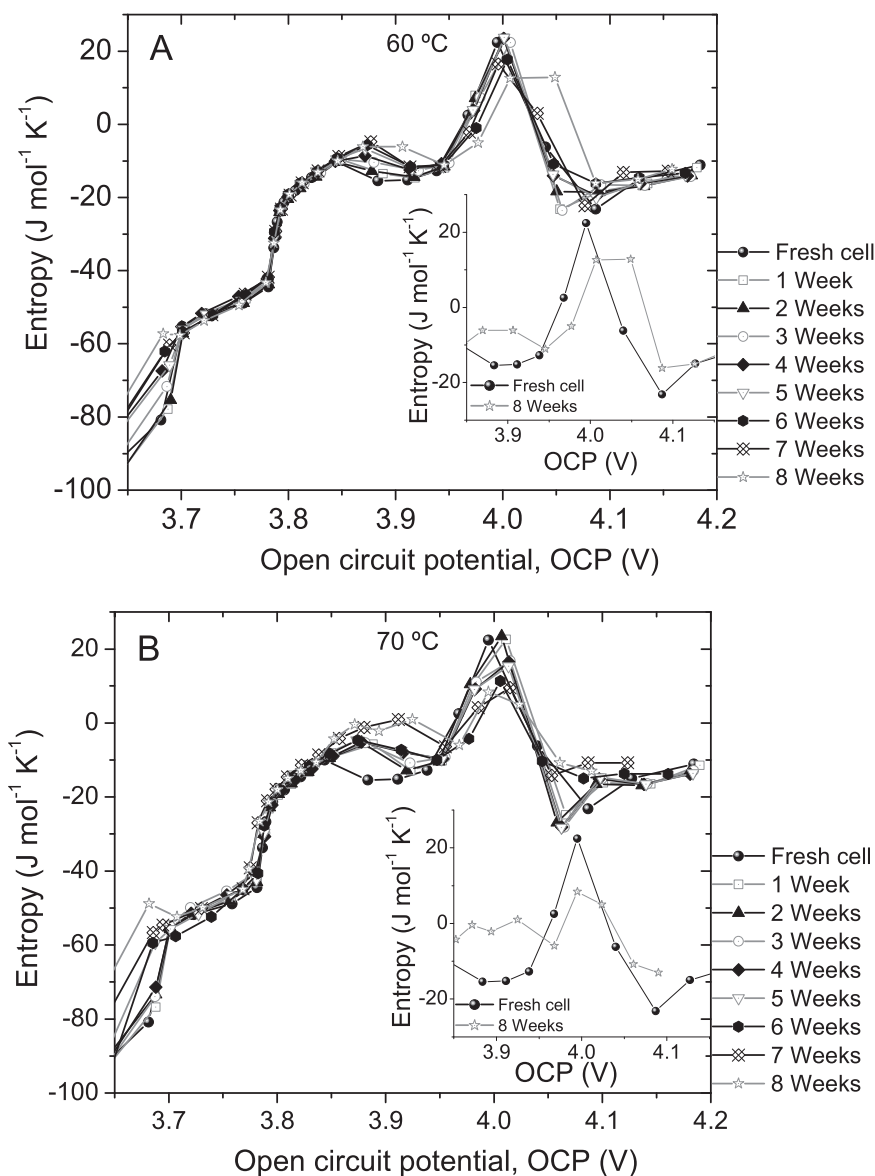


Fig. 6. Entropy profiles vs. OCP of LiB cells aged at (A) 60 °C and, (B) at 70 °C.

energy. The local symmetry around the lithium ions in $\text{Li}_{1-y}\text{CoO}_2$ affects the stability of the material which structure evolves to the lowest energy ground state.

Comparing entropy and enthalpy changes should cast basis for theoretical and experimental materials science research to elucidate their contribution to materials energetics, degradation mechanisms, storage capability, chemical and thermal stability and cycle life. The evolution of thermodynamic properties with the ageing time correlates well with the cells performance but also with the state of health (SOH). SOH as defined in Eq. (5) relates mostly to active vs. inactive components mass ratio in anode and cathode.

3.1.3. Crystal structure characterization

3.1.3.1. LCO cathode. Fig. 10A shows XRD patterns of cathode materials aged at 60 °C for up to 8 weeks and discharged to 2.75 V. For presentation clarity only data taken on samples aged every other week are displayed.

The XRD spectrum of fresh cathode displayed at the bottom of Fig. 10A shows characteristic peaks of pure LiCoO_2 material. This postmortem analysis confirms our earlier statement from entropy and enthalpy data in Figs. 4 and 5 that LiB of this study consist well of LCO cathode material.

To highlight changes in the X-ray diffractograms upon ageing, the areas around the strongest 003 and 104 diffraction peaks are displayed in Fig. 10B and C, respectively. Similarly Fig. 11A–C shows the XRD charts of LCO cathode aged at 70 °C.

Figs. 10B, C and 11B, C show 003 and 104 peaks shifted toward lower angles and broadened. The effects are more pronounced for LCO aged at 70 °C as compared to those at 60 °C for the same ageing time.

A shift to lower angles of the 003 and 104 peaks may result from the presence of small amounts of lithium vacancies in $\text{Li}_{1-y}\text{CoO}_2$, $y \sim 0$ in the fully discharged state of the cells. It is well documented that the 'c' parameter of the LCO hexagonal cell increases with the amounts of lithium vacancies 'y' in $\text{Li}_{1-y}\text{CoO}_2$ in the $0 < y < 0.7$ composition range [46,48,49]. Lithium vacancies in discharged LCO

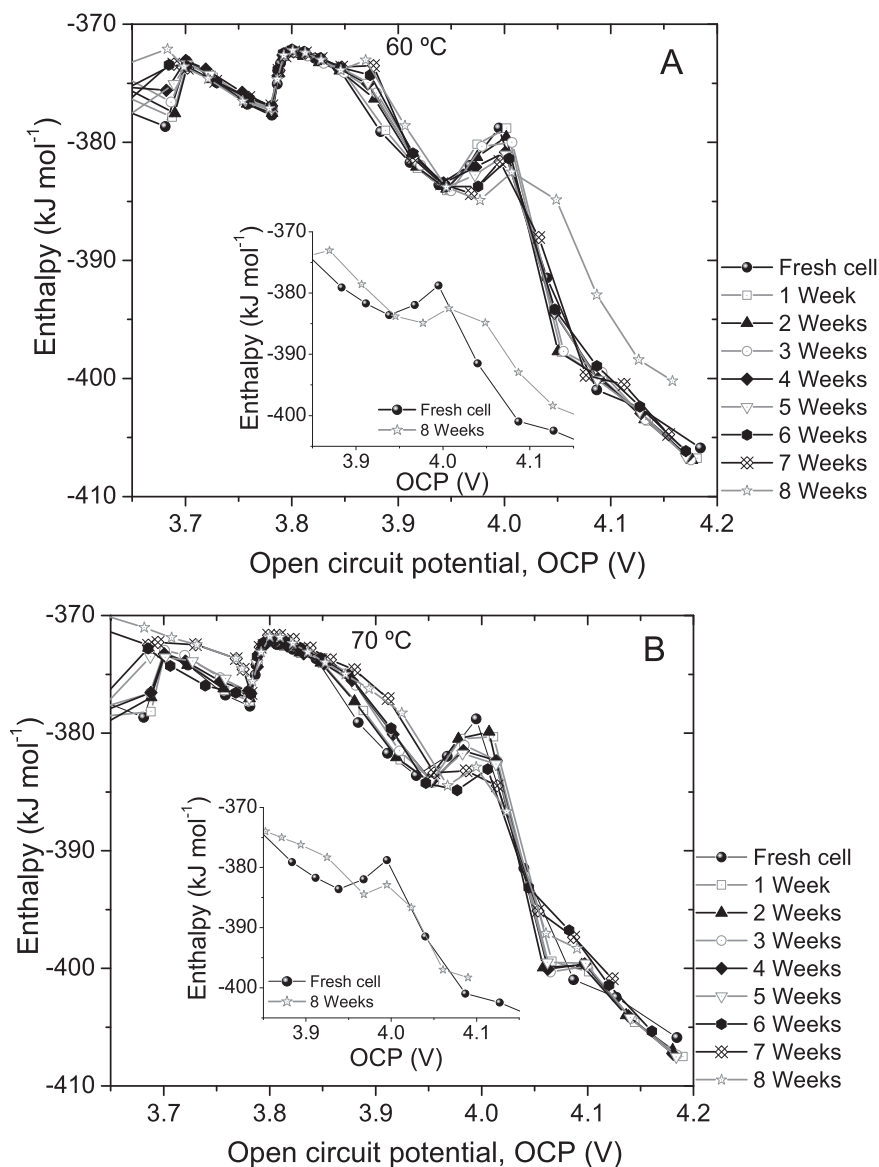


Fig. 7. Enthalpy profiles vs. OCP of LiB cells aged at (A) 60 °C and, (B) at 70 °C.

may result from lithium losses in the graphite anode upon ageing. As will be showed in the following section, residual lithium is trapped in the graphite structure and becomes unavailable. Lithium losses may also result from solid electrolyte interphase (SEI) decomposition and re-formation, which irreversibly consumes lithium stored in the graphite anode.

Because more and more lithium is trapped in the graphite structure and is consumed to form new SEI, the amounts of lithium needed to fully discharge LCO is insufficient and, therefore, the deficiency rate 'y' in discharged cathode increases with ageing time. Accordingly, the 'c' parameter increases as supported by the 003 and 104 peaks shift to lower angles [46,48,49].

Cation mixing in LCO is promoted by both lithium deficiency and a high storage temperature [50,51]. With increasing cation mixing rate, the O3 hexagonal phase eventually converts to cubic spinel phase resulting in 003 and 104 peaks broadening and change in the peaks relative intensity [51]. As a matter of fact in Fig. 12a and b the 104 and 003 peaks intensity ratio I_{104}/I_{003} increases with ageing time at 60 °C and 70 °C, respectively, as result of LCO

conversion from hexagonal to spinel phases [52,53]. The later conversion is further supported by the RS data displayed in Figs. 13 and 14 performed on discharge LCO samples aged at 60 °C and 70 °C, respectively. The RS spectrum of a fresh LCO sample displayed at the bottom of Fig. 13 shows two active modes typical of hexagonal Li_1CoO_2 of $R\bar{3}m$ symmetry, E_g^h and A_{1g}^h at 595 cm^{-1} and 486.7 cm^{-1} , respectively in agreement with the XRD and thermodynamics data [54]. As depicted in Fig. 13 (60 °C) and Fig. 14 (70 °C) upon ageing, new Raman modes appeared and can be assigned to A_{1g}^s and E_g^s modes of spinel LCO (Fd3m symmetry), respectively [55]. Eventually after long ageing time, the spinel peak A_{1g}^s becomes stronger than the hexagonal A_{1g}^h one as shown in Fig. 14. A red shift in E_g^h and A_{1g}^h modes is observed after two weeks ageing at 60 °C and 70 °C. This suggests a decrease in the cation-oxygen bonding energy during ageing has taken place. In the meantime, however, the A_{1g}^s and E_g^s modes remained slightly unchanged within $\pm 1 \text{ cm}^{-1}$ except for the A_{1g}^s mode which decreased from $\sim 699 \text{ cm}^{-1}$ to $\sim 683 \text{ cm}^{-1}$ then to 681 cm^{-1} after 6 and 8 weeks ageing at 70 °C, respectively as reported in Table 1. A red shift in the E_g^h and A_{1g}^h

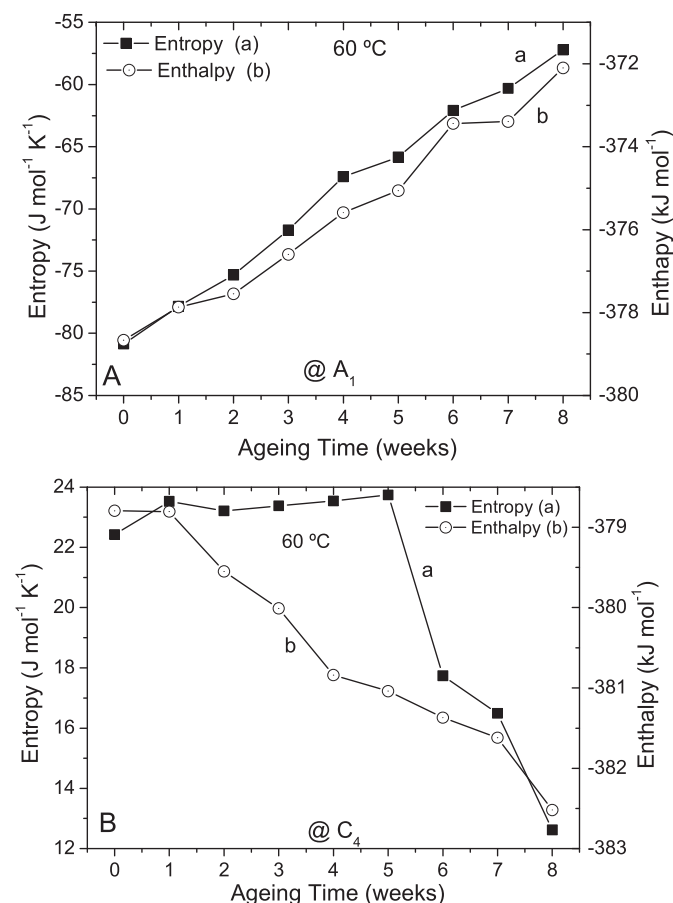


Fig. 8. Time dependence of (a) entropy and, (b) enthalpy of (A) peak A_1 and, (B) peak C_4 of LiB cells aged at 60 °C.

modes may correlate with changes in the enthalpy profiles in Fig. 7A and B underlining a weakening of the M–O bonding energy and/or MO_6 octahedral distortion in the hexagonal phase.

3.1.3.2. Graphite anode. Extended X-ray diffractograms of the anode for different ageing times at 60 °C are shown in Fig. 15A. The diffraction spectrum of fresh anode showed at the bottom of Fig. 15A is typical of graphitic carbon of interlayer spacing of 3.37 Å, which is slightly higher than in highly graphitized carbon (3.35–3.36 Å). XRD data also confirmed our earlier statement from entropy and enthalpy data analyses in Figs. 4 and 5 that LiB cells in this study consist well of a graphite anode.

Fig. 15B shows the 002 peak shifted to lower angles and slightly broadened with the ageing time. A shift of the 002 peak to lower angles should result from residual lithium trapped in the graphite structure and subsequent increase in the interlayer spacing from ~3.37 Å to ~3.40 Å [44]. Similar data are shown in Fig. 17A–B at 70 °C, although with more pronounced effects than in Fig. 16. Residual lithium in discharged graphite anode should occur mainly for kinetics reasons as lithium may become hindered from full de-intercalation due to the SEI becoming more and more resistive with ageing time. The 002 peak broadening relates to increased disorder in the graphite structure, a result in agreement with the RS data shown in Fig. 16. In fact, the RS spectra taken on graphite anodes aged at 60 °C show the two characteristic Raman active modes of graphitic carbon; the G-mode at about 1580 cm^{-1} and the D-mode at about 1350 cm^{-1} [56] changed in relative intensity and in broadening with ageing time. The D-mode is associated with structural defects such as stacking disorder and 2D domains size effects [57].

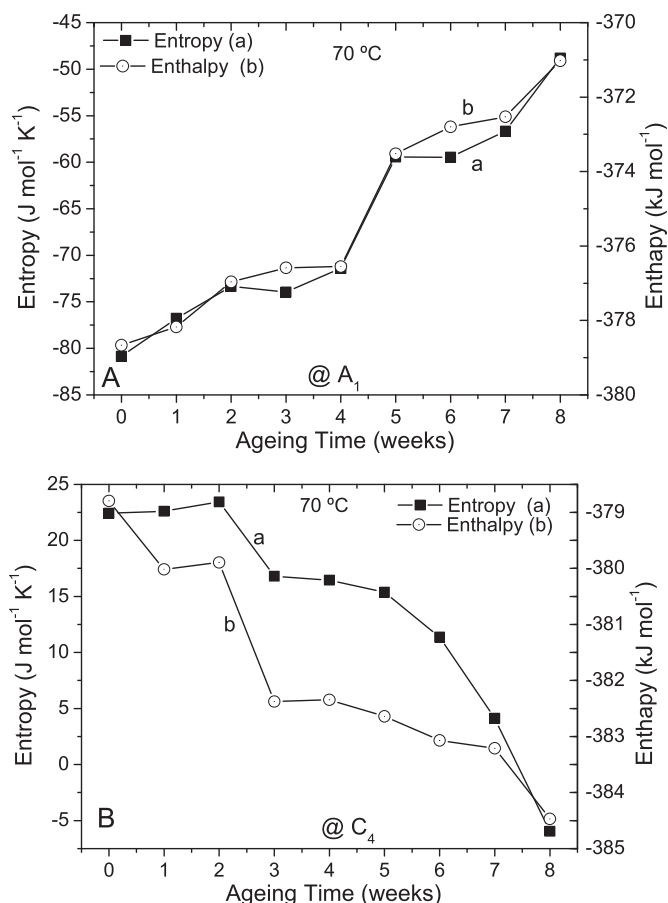


Fig. 9. Time dependence of (a) entropy and, (b) enthalpy of (A) peak A_1 and, (B) peak C_4 of LiB cells aged at 70 °C.

An increase of the D-mode peak intensity relative to G-mode is the signature of enhanced crystal disorder in the graphite anode [58,59].

Fig. 18a and b shows the time dependence of the 002 peak's full-width at half-maximum (FWHM) during ageing at 60 °C and at 70 °C, respectively. As expected the 002 peak broadening is stronger at 70 °C (Fig. 18b) than at 60 °C (Fig. 18a) indicating more structural disordering of the graphite anode with ageing temperature and time. Enhanced disorder in graphite at 70 °C vs. 60 °C is further supported by Raman scattering shown in Fig. 19 achieved on anode sample aged at 70 °C. The D vs. G modes relative intensity ratio is larger in anode aged at 70 °C than at 60 °C as depicted in Fig. 20a and b, respectively. This indicates deeper structural graphite anode degradation has occurred at higher ageing temperatures, a result in agreement with thermodynamics data.

4. Conclusion

We investigated on the effect of thermal ageing of coin lithium ion cells by electrochemical galvanostatic charge and discharge cycling, OCP measurements, entropy and enthalpy profile analysis and by X-ray diffractometry and Raman scattering. We quantified the observed decrease in the electrochemical performances with the ageing temperature and time.

Entropy and enthalpy profiles show more obvious changes with ageing time than the OCP profile. Two particular data points A_1 and C_4 associated with significant changes in entropy and enthalpy profiles in anode and in cathode, respectively, have been revealed and used to monitor electrodes degradation during thermal ageing.

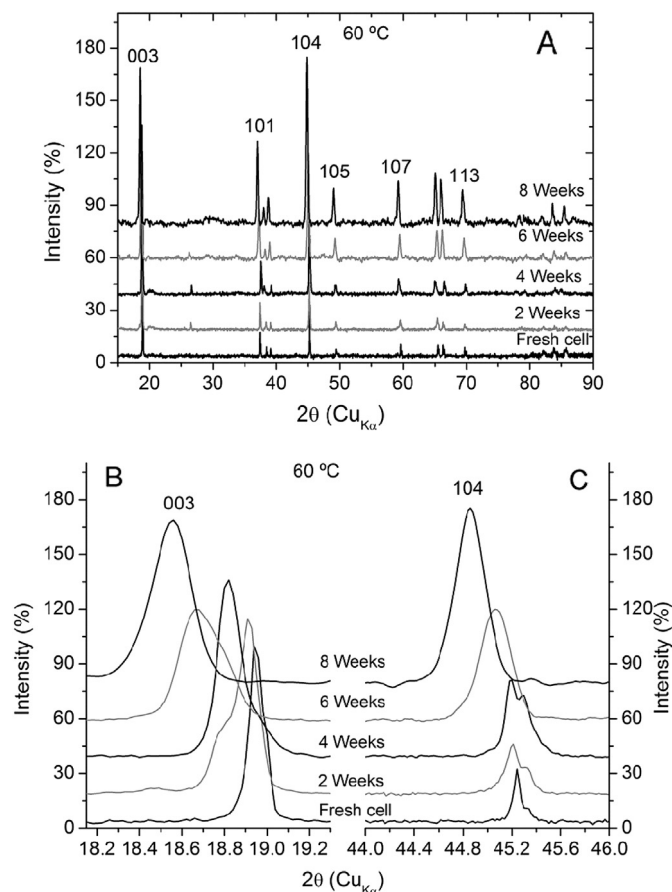


Fig. 10. X-ray diffractograms of LCO cathode material taken from LiB cells aged at 60 °C. (A) full spectra, (B) in the 003 peak area and, (C) in the 104 peak area.

During thermal ageing lithium trapped in the graphite anode and lost during the SEI formation and decomposition cycle accounts for most of the irreversible consumption of active lithium in the cell and, therefore, to lithium deficiencies in the discharged LCO cathode and to irreversible capacity loss. Furthermore, lithium deficiency in LCO leads to cation mixing and eventually to hexagonal to spinel irreversible phase conversion, a result confirmed by thermodynamics data and by post mortem XRD and RS analyses.

By assigning onsets of phase transitions in the entropy and enthalpy profiles specifically to anode (A_1) and cathode (C_4) our thermodynamics method allows a clear distinction between contribution to the cell performance decay originating from each one of the electrodes. This feature is a direct consequence of the “electrochemical signal amplifier effect” of entropy and enthalpy functions at phase transitions as compared to more commonly used Gibbs energy (or OCP) function.

Differences in thermodynamic behaviour in anode and cathode were revealed in this study. In anode entropy and enthalpy increased in a correlated way, whereas in cathode, entropy and enthalpy generally decreased uncorrelated. Changes in entropy and enthalpy in anode go with graphene layers stacking disorder, whereas in cathode, changes go with the LCO irreversible conversion from hexagonal to spinel structure.

Compared to our previous studies on LiB ageing upon over-charge [41] and long cycling [42], we found thermal ageing to affect anode and cathode crystal structure degradation quite differently. In particular cells having sustained same capacity loss under different ageing conditions show different thermodynamics properties, which relate to differences in electrode degradation rates.

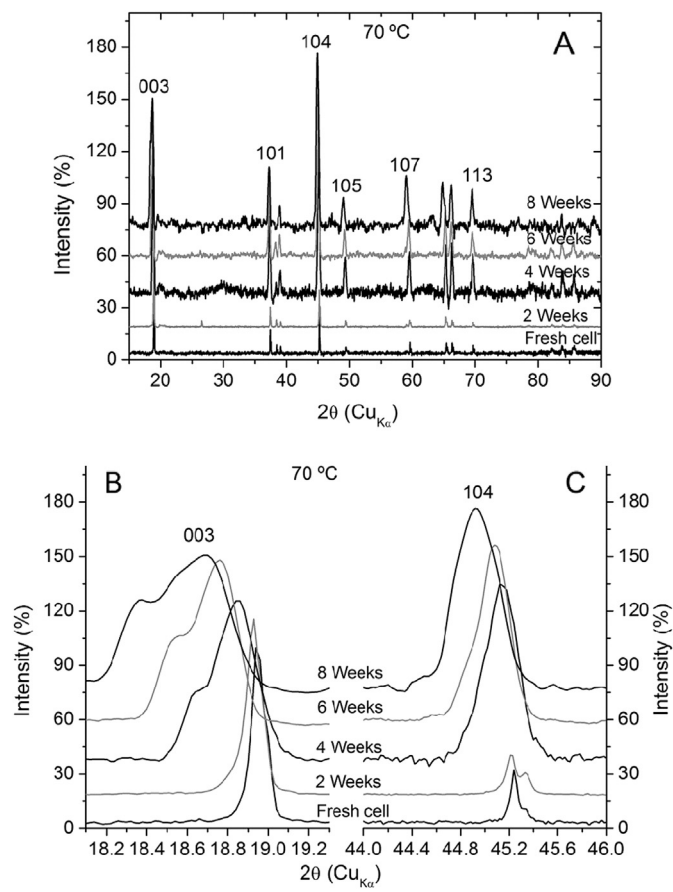


Fig. 11. X-ray diffractograms of LCO cathode material taken from LiB cells aged at 70 °C. (A) full spectra, (B) in the 003 peak area and, (C) in the 104 peak area.

Our thermodynamics analytical method is novel, non-destructive and is complementary to other costly and bulky in-situ investigation tools such XRD, neutron scattering, X-ray absorption spectrometry, etc. Thermodynamics methods apply to any battery chemistry as long as OCP, Σ and T are measured accurately. Applications include accurate assessment of phase diagrams of anode and cathode together with investigations on battery

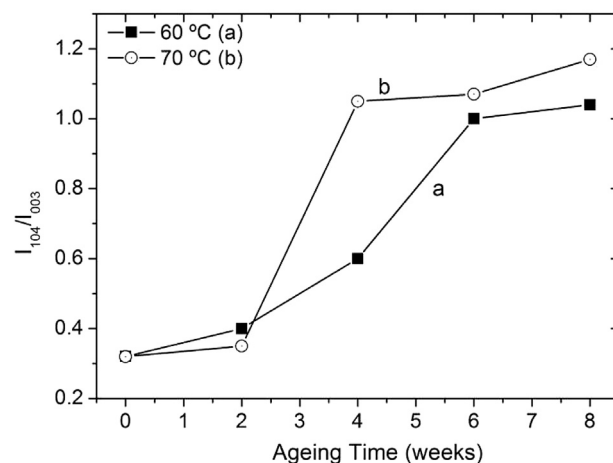


Fig. 12. Time dependence of 104/003 peak intensity ratio of LCO cathode materials taken from LiB cells aged at (a) 60 °C and, (b) 70 °C.

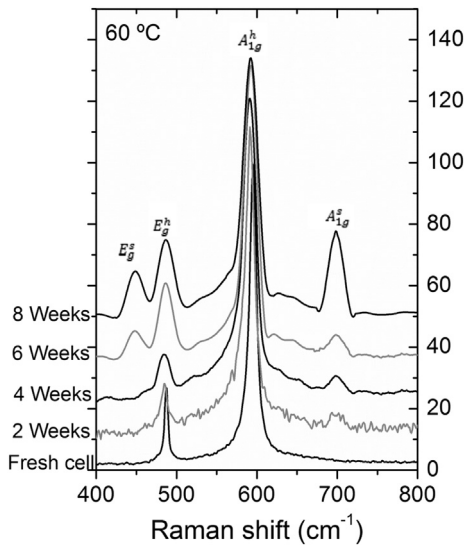


Fig. 13. Time dependence of Raman scattering spectra of LCO cathode materials taken from LiB cells aged at 60 °C.

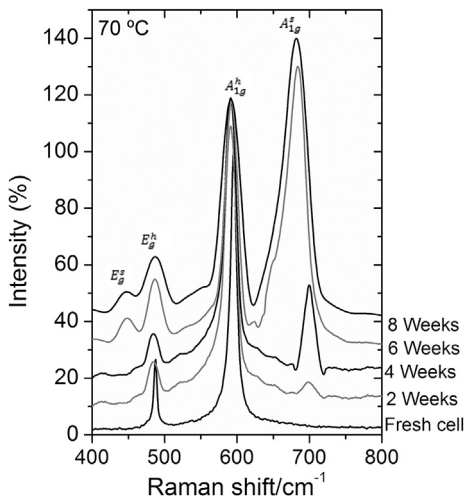


Fig. 14. Time dependence of Raman scattering spectra of LCO cathode materials taken from LiB cells aged at 70 °C.

Table 1
Raman active modes in LCO cathode upon ageing at 60 °C and 70 °C for up to 8 weeks at initial charge state of 4.2 V.

Ageing time at 60 °C (Week)	E _g ^s /cm ^{-1a}	E _g ^h /cm ^{-1a}	A _{1g} ^h /cm ⁻¹	A _{1g} ^s /cm ⁻¹
0	—	486.7	595	—
2	—	484.3	591.5	698.3
4	—	484.3	591.5	699.5
6	447.4	486.7	592.6	699.5
8	448.7	486.7	592.6	699.5

Ageing time at 70 °C (Week)	Peak1/cm ⁻¹	Peak2 (E _g)/cm ⁻¹	Peak2 (A _{1g})/cm ⁻¹	Peak4/cm ⁻¹
0	—	486.7	595	—
2	—	483.1	591.5	698.3
4	—	484.3	592.6	699.5
6	447.5	486.7	591.5	683.3
8	446.3	486.7	591.5	681

^a s and h relate to spinel and hexagonal symmetry phases, respectively.

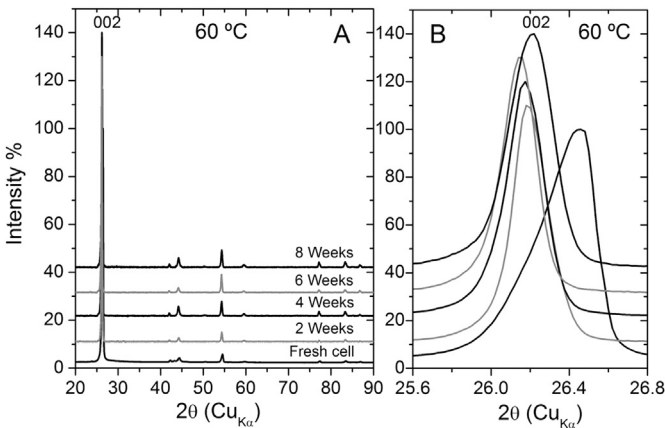


Fig. 15. X-ray diffractograms of graphite anode material taken from LiB cells aged at 60 °C, (A) full spectra and, (B) in the 002 peak area.

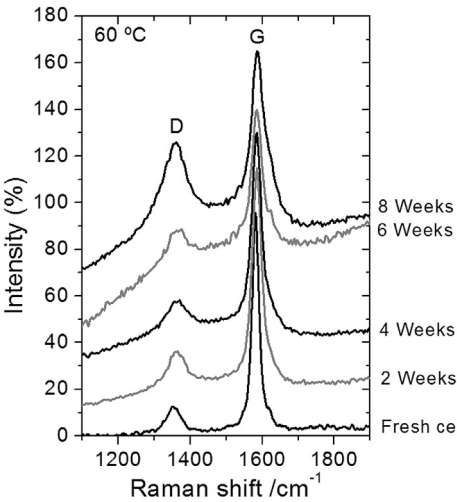


Fig. 16. Time dependence of Raman scattering spectra of graphite anode materials taken from LiB cells aged at 60 °C.

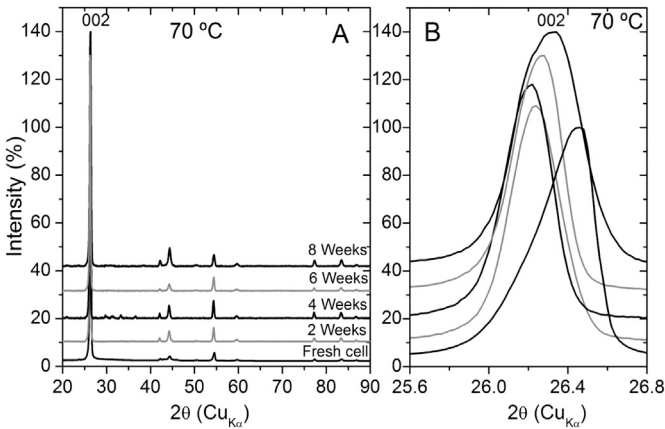


Fig. 17. X-ray diffractograms of graphite anode material taken from LiB cells aged at 70 °C, (A) full spectra and, (B) in the 002 peak area.

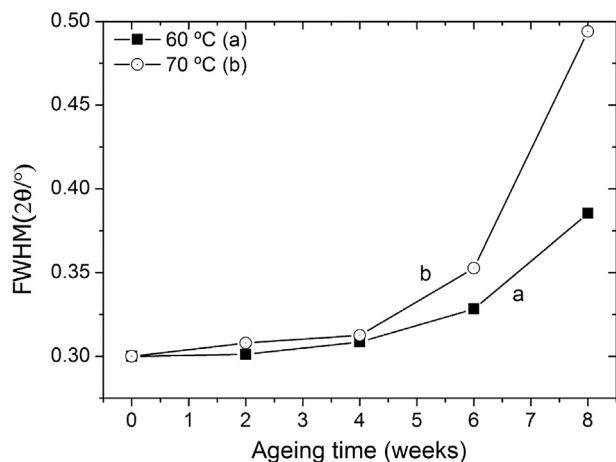


Fig. 18. Time dependence of the graphite anode 002 peak full-width at half-maximum (FWHM) during ageing at (a) 60 °C and, (b) 70 °C.

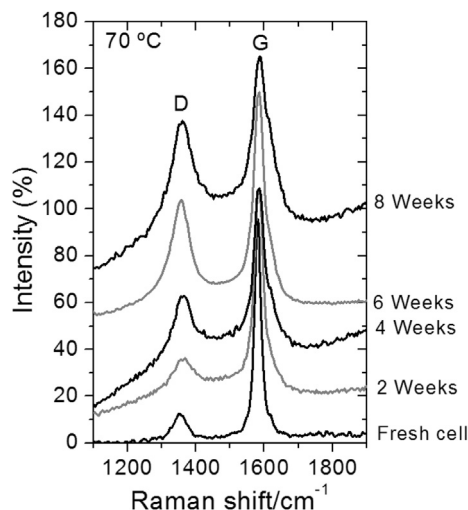


Fig. 19. Time dependence of Raman scattering spectra of graphite anode materials taken from LiB cells aged at 70 °C.

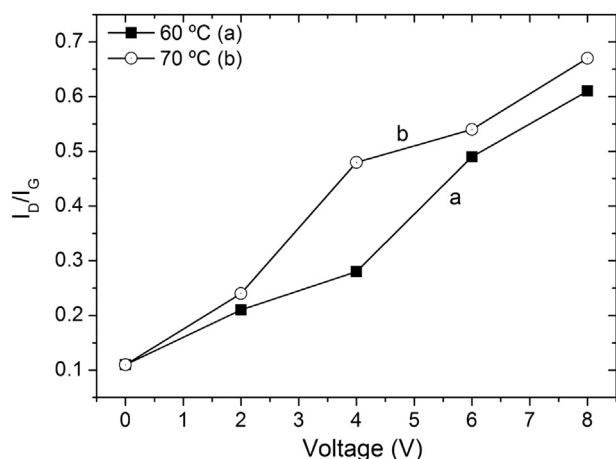


Fig. 20. Time dependence of D-mode and G-mode peak intensity ratio of graphite anode materials taken from LIB cells aged at (a) 60 °C and, (b) 70 °C.

performance degradation mechanisms and battery state of health and more crucial state of safety assessments.

Acknowledgements

The authors would like to thank Mrs. Olivia Wijaya and Mrs. Hong Yu for their help in performing the Raman experiments.

References

- [1] P. Ramadass, B. Haran, R. White, B.N. Popov, J. Power Sources 112 (2002) 606.
- [2] K. Takei, K. Kumai, Y. Kobayashi, H. Miyashiro, N. Terada, T. Iwahori, T. Tanaka, J. Power Sources 97–98 (2001) 697.
- [3] K. Sawai, R. Yamato, T. Ohzuku, Electrochim. Acta 51 (2006) 1651.
- [4] J.R. Belt, C.D. Ho, T.J. Miller, M.A. Habib, T.Q. Duong, J. Power Sources 142 (2005) 354.
- [5] K. Amine, J. Liu, I. Belharouak, Electrochem. Commun. 7 (2005) 669.
- [6] E.V. Thomas, H.L. Case, D.H. Doughty, R.G. Jungst, G. Nagasubramanian, E.P. Roth, J. Power Sources 124 (2003) 254.
- [7] G.M. Ehrlich, in: D. Linden, T.B. Reddy (Eds.), Handbook of Batteries, third ed., McGraw-Hill, New York, 2002, p. 35.1.
- [8] K. Asakura, M. Shimomura, T. Shodai, J. Power Sources 119 (2003) 902.
- [9] R.P. Ramasamy, R.E. White, B.N. Popov, J. Power Sources 141 (2005) 298.
- [10] T. Horiba, T. Maeshima, F. Matsumura, M. Koseki, J. Arai, Y. Muranaka, J. Power Sources 146 (2005) 107.
- [11] I. Bloom, B.W. Cole, J.J. Sohn, S.A. Jones, E.G. Polzin, V.S. Battaglia, G.L. Henriksen, C. Motloch, R. Richardson, T. Unkelhaeuser, D. Ingersoll, H.L. Case, J. Power Sources 101 (2001) 238.
- [12] A.M. Lackner, E. Sherman, P.O. Braatz, J.D. Margerum, J. Power Sources 104 (2002) 1.
- [13] M. Dubarry, B.Y. Liaw, M.S. Chen, S.S. Chyan, K.C. Han, W.T. Sie, S.H. Wu, J. Power Sources 196 (2011) 3420.
- [14] J. Li, E. Murphy, J. Winnick, P.A. Kohl, J. Power Sources 102 (2001) 294.
- [15] Y.H. Ye, Y.X. Shi, N.S. Cai, J. Lee, X.M. He, J. Power Sources 199 (2012) 227.
- [16] K.C. Lim, A.M. Lackner, P.O. Braatz, W.H. Smith, J.D. Margerum, H.S. Lim, in: Proceedings of the Symposium Batteries for Portable Applications and Electric Vehicles, vol. 97–181, The Electrochemical Society, Paris, France, 31 August–5 September, 1997, p. 470.
- [17] J. Vetter, P. Novak, M.R. Wagner, C. Veit, K.C. Moller, J.O. Besenhard, M. Winter, M. Wohlfahrt-Mehrens, C. Vogler, A. Hammouche, J. Power Sources 147 (2005) 269.
- [18] S.S. Choi, H.S. Lim, J. Power Sources 111 (2002) 130.
- [19] R.A. Leising, M.J. Palazzo, E.S. Takeuchi, K.J. Takeuchi, J. Power Sources 97 (2001) 681.
- [20] W. Lu, C.M. Lopez, N. Liu, J.T. Vaughey, A. Jansen, D.W. Dees, J. Electrochem. Soc. 159 (2012) A566.
- [21] M. Broussely, in: W.A.V. Schalkwijk, B. Scrosati (Eds.), Advances in Lithium-ion Batteries, Kluwer Academic/Plenum Publishers, New York, 2002, p. 393.
- [22] S. Santhanagopalan, Q. Zhang, K. Kumaresan, R.E. White, J. Electrochem. Soc. 155 (2008) A345.
- [23] P. Ramadass, B. Haran, R. White, B.N. Popov, J. Power Sources 111 (2002) 210.
- [24] R. Kosteki, F. McLarnon, J. Power Sources 119 (2003) 550.
- [25] E. Markevich, G. Salitra, M.D. Levi, D. Aurbach, J. Power Sources 146 (2005) 146.
- [26] J. Li, J. Zhang, X. Zhang, C. Yang, N. Xu, B. Xia, Electrochim. Acta 55 (2010) 927.
- [27] D.P. Abraham, J. Liu, C.H. Chen, Y.E. Hyung, M. Stoll, N. Elsen, S. MacLaren, R. Twisten, R. Haasch, E. Sammann, I. Petrov, K. Amine, G. Henriksen, J. Power Sources 119–121 (2003) 511.
- [28] Y.J. Park, J.W. Lee, Y.G. Lee, K.M. Kim, M.G. Kang, Y. Lee, Bull. Korean Chem. Soc. 28 (2007) 2226.
- [29] Y. Matsumura, S. Wang, J. Mondori, J. Electrochem. Soc. 142 (1995) 2914.
- [30] P. Arora, R.E. White, M. Doyle, J. Electrochem. Soc. 145 (1998) 3647.
- [31] G. Ning, B.N. Popov, J. Electrochem. Soc. 151 (2004) A1584.
- [32] R.J. Gummow, A. de Kock, M.M. Thackeray, Solid State Ionics 69 (1994) 59.
- [33] J.M. Tarascon, W.R. McKinnon, F. Coowar, T.N. Bowmer, G. Amatucci, D. Guyomard, J. Electrochem. Soc. 141 (1994) 1421.
- [34] S. Choi, A. Manthiram, J. Electrochem. Soc. 153 (2002) A1760.
- [35] G. Pistoia, A. Antonini, R. Rosati, D. Zane, Electrochim. Acta 41 (1996) 2683.
- [36] D. Aurbach, K. Gamolsky, B. Markowsky, G. Salitra, Y. Gofer, U. Heider, R. Oesten, M. Schmidt, J. Electrochem. Soc. 147 (2000) 1322.
- [37] D. Aurbach, E. Zinigrad, Y. Cohen, H. Teller, Solid State Ionics 148 (2002) 405.
- [38] D. Aurbach, B. Markowsky, A. Rodkin, M. Cojocar, E. Levi, H.J. Kim, Electrochim. Acta 47 (2002) 1899.
- [39] M.C. Smart, B.V. Ratnakumar, S. Surampudi, Y. Wang, X. Zhang, B. Fultz, J. Electrochem. Soc. 146 (1999) 3963.
- [40] F. Bonhomme, Ph. Biensan, C. Jordy, D. Germond, J.M. Lalluque, M. Broussely, C. Delmas, L. Croguennec, M. Menetrier, C. Vaysse, in: Proceedings of the IBA Meeting, Graz, 2004.
- [41] K. Maher, R. Yazami, Electrochim. Acta 101 (2013) 71.
- [42] K. Maher, R. Yazami, J. Power Sources 247 (2014) 527.
- [43] R. Yazami, in: K. Ozawa (Ed.), Lithium Ion Rechargeable Batteries, Materials, Technology and New Applications, Wiley-VCH, Weinheim, 2009, p. 67.

- [44] D. Billaud, F. Henry, P. Willmann, *Mol. Cryst. Liq. Cryst.* 244 (1994) 159.
- [45] Y.F. Reynier, R. Yazami, B. Fultz, *J. Electrochem. Soc.* 151 (2004) A422.
- [46] Z. Chen, J.R. Dahn, *Electrochim. Acta* 49 (2004) 1079.
- [47] Y. Reynier, J. Gaetz, T. Swan-Wood, P. Rez, R. Yazami, B. Fultz, *Phys. Rev. B* 70 (2004) 174304.
- [48] T. Ohzuku, A. Ueda, *J. Electrochem. Soc.* 141 (1994) 2972.
- [49] G.G. Amatucci, J.M. Tarascon, L.C. Klein, *J. Electrochem. Soc.* 143 (1996) 1114.
- [50] Z. Chen, Z. Lu, J.R. Dahn, *J. Electrochem. Soc.* 149 (2002) A1604.
- [51] Y. Ozawa, R. Yazami, B. Fultz, *J. Power Sources* 119 (2003) 918.
- [52] H. Gabrisch, R. Yazami, B. Fultz, *J. Electrochem. Soc.* 151 (2004) A891.
- [53] R. Gupta, A. Manthiram, *J. Solid State Chem.* 121 (1996) 483.
- [54] J. Kim, P. Fulmer, A. Manthiram, *Mater. Res. Bull.* 34 (1999) 571.
- [55] L. Mendoza, R. Baddour-Hadjean, M. Cassir, J.P. Pereira-Ramos, *Appl. Surf. Sci.* 225 (2004) 356.
- [56] C. Julien, *Solid State Ionics* 136–137 (2000) 887.
- [57] F. Tuinstra, J. Koenig, *J. Chem. Phys.* 53 (1970) 1126.
- [58] M.A. Pimenta, G. Dresselhaus, M.S. Dresselhaus, L.G. Cancado, A. Jorio, R. Saito, *Phys. Chem. Chem. Phys.* 9 (2007) 1276.
- [59] L.J. Hardwick, M. Marcinek, L. Beer, J.B. Kerr, R. Kostecki, *J. Electrochem. Soc.* 155 (2008) A442.